

BLAST: A FAR-INFRARED MEASUREMENT OF THE HISTORY OF STAR FORMATION

ENZO PASCALE¹, PETER A. R. ADE¹, JAMES J. BOCK², EDWARD L. CHAPIN³, MARK J. DEVLIN⁴, SIMON DYE¹,
STEVE A. EALES¹, MATTHEW GRIFFIN¹, JOSHUA O. GUNDERSEN⁵, MARK HALPERN³, PETER C. HARGRAVE¹,
DAVID H. HUGHES⁶, JEFF KLEIN⁴, GAELLEN MARSDEN³, PHILIP MAUSKOPF¹, LORENZO MONCELSI¹,
CALVIN B. NETTERFIELD^{7,8}, LUCA OLMI^{9,10}, GUILLAUME PATANCHON¹¹, MARIE REX⁴, DOUGLAS SCOTT³,
CHRISTOPHER SEMISCH⁴, NICHOLAS THOMAS⁵, MATTHEW D. P. TRUCH⁴, CAROLE TUCKER¹, GREGORY S. TUCKER¹²,
MARCO P. VIERO⁸ & DONALD V. WIEBE^{3,8}

To appear in the Astrophysical Journal

ABSTRACT

We use measurements from the Balloon-borne Large Aperture Sub-millimeter Telescope (BLAST) at wavelengths spanning 250 to 500 μm , combined with data from the *Spitzer* Infrared telescope and ground-based optical surveys in GOODS-S, to determine the average star formation rate of the galaxies that comprise the cosmic infrared background (CIB) radiation from 70 to 500 μm , at redshifts $0 < z < 3$. We find that different redshifts are preferentially probed at different wavelengths within this range, with most of the 70 μm background generated at $z \lesssim 1$ and the 500 μm background generated at $z \gtrsim 1$. The spectral coverage of BLAST and *Spitzer* in the region of the peak of the background at $\sim 200 \mu\text{m}$ allows us to directly estimate the mean physical properties (temperature, bolometric luminosity and mass) of the dust in the galaxies responsible for contributing more than 80% of the CIB. By utilizing available redshift information we directly measure the evolution of the far infrared luminosity density and therefore the optically obscured star formation history up to redshift $z \sim 3$.

Subject headings: cosmology: observations — cosmology: diffuse radiation — submillimeter — galaxies: evolution — galaxies: starburst

1. INTRODUCTION

The spectrum of the diffuse extragalactic background radiation reflects the physical processes that have dominated the evolution of the Universe. The Cosmic Microwave Background, the relic radiation of the Big Bang, is the dominant contribution. The second most important component spans the optical to far-infrared part of the spectrum, with roughly equal energy in broad peaks at around 200 μm and 1 μm . This component is due to the light emitted by stars throughout cosmic time. In the far infrared (FIR), the source of the Cosmic Infrared Background (CIB) is warm dust which enshrouds star-forming regions in galaxies; thus, a detailed account of

the CIB is needed to understand the history of star formation in the Universe (e.g. Dwek et al. 1998). The CIB was first detected with the FIRAS and DIRBE instruments on board the *COBE* satellite (Puget et al. 1996; Fixsen et al. 1998). By resolving the contribution from individual sources to the CIB as a function of redshift, it should be possible to determine the FIR history of the Universe which is closely related to the history of star and galaxy formation.

The current class of FIR and submillimeter experiments, including the SPIRE (Griffin et al. 2003) instrument on the *Herschel* satellite, cannot resolve the CIB into individually detected sources because of confusion arising from the finite instrumental angular resolution. To date, the CIB has been resolved into 24 μm , 850 μm , and 1.1 mm detected sources, but the background is several tens of times smaller at these wavelengths than it is at its peak. It is, however, possible to study the contribution that a given class of objects makes to the background with a stacking analysis consisting of calculating the covariance of known source positions with maps from these experiments. This approach has been successfully used by many authors (e.g. Dole et al. 2006; Dye et al. 2007; Devlin et al. 2009). Marsden et al. (2009) details the mathematical background of this formalism.

Individual sources brighter than 60 μJy detected in deep surveys with the Multiband Imaging Photometer for *Spitzer* (MIPS) at 24 μm resolve most of the CIB at 24 μm ($\sim 70\%$, Papovich et al. 2004). Stacking analyses have shown that these sources also constitute a large fraction of the background at 70 and 160 μm ($\sim 80\%$, Dole et al. 2006). Recently, Devlin et al. (2009) obtained a similar result from 250 to 500 μm with the Balloon-Borne Large Aperture Submillimeter Telescope, BLAST

¹ School of Physics & Astronomy, Cardiff University, 5 The Parade, Cardiff, CF24 3AA, UK; enzo.pascale@astro.cf.ac.uk.

² Jet Propulsion Laboratory, Pasadena, CA 91109-8099, USA.

³ Department of Physics & Astronomy, University of British Columbia, 6224 Agricultural Road, Vancouver, BC V6T 1Z1, Canada.

⁴ Department of Physics & Astronomy, University of Pennsylvania, 209 South 33rd Street, Philadelphia, PA, 19104, USA.

⁵ Department of Physics, University of Miami, 1320 Campo Sano Drive, Coral Gables, FL 33146, USA.

⁶ Instituto Nacional de Astrofísica Óptica y Electrónica (INAOE), Aptdo. Postal 51 y 72000 Puebla, Mexico.

⁷ Department of Astronomy & Astrophysics, University of Toronto, 50 St. George Street Toronto, ON M5S 3H4, Canada.

⁸ Department of Physics, University of Toronto, 60 St. George Street, Toronto, ON M5S 1A7, Canada.

⁹ University of Puerto Rico, Rio Piedras Campus, Physics Dept., Box 23343, UPR station, Puerto Rico 00931.

¹⁰ INAF, Osservatorio Astrofisico di Arcetri, Largo E. Fermi 5, I-50125, Firenze, Italy.

¹¹ Université Paris Diderot, Laboratoire APC, 10, rue Alice Domon et Léonie Duquet 75205 Paris, France.

¹² Department of Physics, Brown University, 182 Hope Street, Providence, RI 02912, USA.

(Pascale et al. 2008), and found that the background resolved by sources detected in the deepest MIPS images at $24\ \mu\text{m}$ is compatible with the FIRAS measurements within the $1\ \sigma$ errors. While the FIRAS measurements of the CIB in the submillimeter are uncertain at the level of 25%, it is now becoming clear that most of it is accounted for by $24\ \mu\text{m}$ selected sources whose redshift distribution has a median of $z \sim 0.9$ (§3). It is certainly possible that a population with fainter $24\ \mu\text{m}$ flux densities is missing, probably associated with the submillimeter galaxies detected by SCUBA and MAMBO. These massive star-forming galaxies dominate the star formation rate at $z \sim 2.5$ and the CIB at $850\ \mu\text{m}$ and $1.1\ \text{mm}$, but contribute relatively little to the peak of the CIB (Dye et al. 2007). Further investigation of the contribution of $24\ \mu\text{m}$ selected sources to the background is proving to be an effective way to study the statistical properties of the CIB.

BLAST has observed an $8.7\ \text{deg}^2$ region encompassing the Extended Chandra Deep Field South (ECDFS) and Great Observatories Origins Deep Survey South (GOODS-S). Additional time was spent observing a smaller $0.9\ \text{deg}^2$ area at the center of this field, though the coverage is still broader than most of the other deep data available at other wavelengths. We refer to these fields as BLAST GOODS-S Wide (BGS-Wide) and BLAST GOODS-S Deep (BGS-Deep) respectively. We note that BGS-Deep is dominated by the confusion from point sources arising from the $36''$ – $60''$ BLAST beams, rather than instrumental noise.

Observing in three broad bands centered at 250 , 350 , and $500\ \mu\text{m}$, BLAST provides a new data set of unique size, resolution, and spectral coverage to study the properties of the CIB on the submillimeter side of its maximum. Together with MIPS observations at $70\ \mu\text{m}$, it is now possible to constrain the CIB without assumptions about any of the physical properties of the sources contributing to it.

The BLAST surveys in BGS-Wide and Deep have now been used in several studies. Devlin et al. (2009) estimate the number counts of the submillimeter sources at BLAST wavelengths, in addition to studying the contribution from sources selected at $24\ \mu\text{m}$, in the radio, and in the soft and hard X-rays to the CIB. Marsden et al. (2009) examine in greater detail the contribution from MIPS sources to the CIB, extending the results of Devlin et al. (2009), and showing that most of the CIB light originates at redshifts $z > 1.2$. Dye et al. (2009) find MIR and radio counterparts for a sample of bright BLAST sources and measure their redshift distribution. In this work we present a detailed analysis of all sources that contribute significantly to the CIB at $70\ \mu\text{m}$, $250\ \mu\text{m}$, $350\ \mu\text{m}$, and $500\ \mu\text{m}$ as a function of redshift, even those well below the confusion limit. From this we derive the evolutionary history of the CIB, which is intimately related to the FIR history of star formation. The results from these four analysis papers will be used by Chapin et al. (in preparation) to infer the evolution of the FIR luminosity function.

A portion of the BGS-Deep region has been surveyed at many wavelengths from which we derived an almost complete set of redshifts ($\sim 95\%$) for MIPS sources. By exploiting BLAST and MIPS $70\ \mu\text{m}$ data, we estimate the

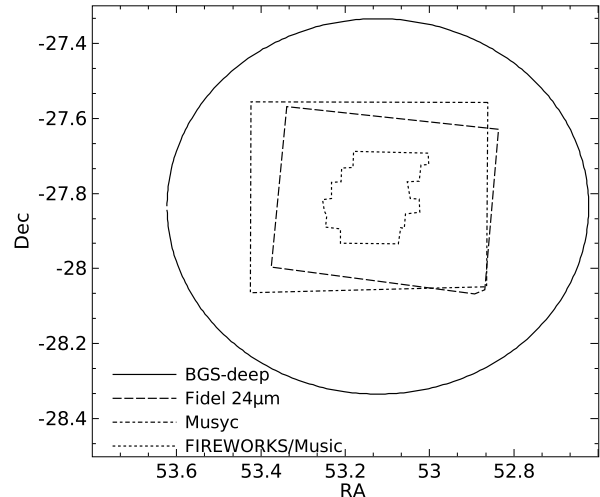


FIG. 1.— Extent of the catalogs in the BGS-Deep region observed with BLAST. The area used for the stacking analysis is the intersection of the FIDEL and MUSYC regions and extends over $590\ \text{arcmin}^2$.

mean physical parameters for these galaxies (bolometric luminosities, temperatures, and dust masses), and the total FIR luminosity evolution and star formation history of the Universe. Our results are in good agreement with existing measurements. We find that stars form in optically obscured dusty galaxies at rates ~ 3 times larger than those previously estimated in the optical at redshifts up to $z \sim 1$. We also estimate the total comoving dust mass density with redshift, finding no sign of evolution within the experimental uncertainties, over the range $z \lesssim 3$.

A flat cosmological model with $\Omega_\Lambda = 0.7$, $h = 0.7$ has been used throughout.

2. DATA

In this section we describe each of the data sets used. Their locations and angular extents are depicted in Figure 1.

2.1. BLAST Submillimeter Imaging

The BGS-Deep region observed with BLAST covers the central $0.9\ \text{square degrees}$ of a shallower map imaging the full $8.7\ \text{deg}^2$ area in BGS-Wide.

The raw time ordered data (TOD), consisting of a set of voltage time-streams from each of the BLAST detectors, are pre-processed (Truch et al. 2008; Patanchon et al. 2008). Any corrupt samples are flagged, and the data are deconvolved using the instrumental transfer functions. The TODs are binned into maps using the telescope pointing solution (Pascale et al. 2008) which has an estimated RMS positional error of less than $5''$ (Marsden et al. 2008). The absolute photometric calibration has an estimated accuracy of $\sim 10\%$, which is highly correlated across the BLAST bands (Truch et al. 2009). Calibration errors and color corrections are accounted for in our SED fits.

The maps used in this work have been generated using OptBin (Pascale et al. in preparation). The algorithm performs common-mode suppression and high-pass filters the output above the low-frequency “knee” of the detector noise (Pascale et al. 2008). The filtered data

streams are then projected onto a map. This treatment is appropriate for point source extraction as it does not distort the data on timescales comparable to the beam-crossing times. OptBin reduces the 100 hour long BGS-Wide data-set at $250\ \mu\text{m}$ in one hour on a single-CPU machine, and it is also used as part of an end-to-end instrumental simulator which allows Monte Carlo analysis.

Results have been compared and found to be compatible with those obtained using maps reduced with the more computationally intensive SANEPIC (Patanchon et al. 2008), which provides the least-squares solution to the map-making equation.

2.2. Spitzer Data

Extensive *Spitzer* maps cover most of the BGS-Deep and Wide regions. The *Spitzer* Wide-Area Infrared Extragalactic Survey (SWIRE, Lonsdale et al. 2003, data release 3), provides $\sim 7.5\ \text{deg}^2$ maps well matched to the BGS-Wide coverage. We use the BLAST data in conjunction with the $70\ \mu\text{m}$ SWIRE data to constrain the brightness of the peak in the CIB.

Deep imaging of this field is available in the four IRAC (Infrared Array Camera) bands from the SIMPLE (*Spitzer*'s IRAC and MUSYC Public Legacy of the ECDFS, Damen et al. 2009) survey. MIPS data from the *Spitzer* Far-Infrared Deep Extragalactic Legacy (FIDEL) survey is also available. The catalog of $24\ \mu\text{m}$ sources detected in the FIDEL maps is the same used by Devlin et al. (2009) and Marsden et al. (2009), and uses the IRAC sources detected in SIMPLE as a positional prior.

The faintest $24\ \mu\text{m}$ source in the catalog has a flux density of $13\ \mu\text{Jy}$, but the detections at $S_{24} < 30\ \mu\text{Jy}$ should be considered tentative. The catalog includes 9110 sources covering $700\ \text{arcmin}^2$, with IRAC flux densities (at 3.6, 4.5, 5.8, and $8\ \mu\text{m}$) available for each entry.

2.3. Optical Photometric Redshifts

We use five different catalogs of photometric redshifts available in the BGS-Deep region to assign a redshift to the majority of the MIR sources in the FIDEL catalog.

Brammer et al. (2008) released two catalogs of photometric redshifts in the BGS-Deep region using MUSYC (MULTIWavelength Survey by Yale-Chile, Taylor et al. 2009) and FIREWORKS (Wuyts et al. 2008) imaging data, calculated with a new algorithm called EAZY. EAZY performs linear combinations of SED templates to find the best fits to measured photometry, which in these two cases span the optical (*UBVRI*) and the IR (*JHK*), as well as the 4 IRAC bands. They provide values for the Q_z statistic which indicates the confidence level associated with the inferred redshifts. As explained therein, redshifts with $Q_z < 3$ result in a statistical error of $\sigma_z \equiv \Delta z / (1 + z) < 0.1$. Whenever the Q_z statistic is available, we select redshifts using this cut. The MUSYC catalog covers an area of $900\ \text{arcmin}^2$ and contains ~ 17000 sources, while FIREWORKS extends over a $140\ \text{arcmin}^2$ area and has ~ 6300 sources. The typical redshift errors are $\sigma_z \lesssim 0.04$.

The GOODS-MUSIC (Grazian et al. 2006) catalog contains ~ 15000 sources in a region overlapping FIREWORKS. About 6.5% of the redshifts listed in the catalog are spectroscopic, and the others are photometric

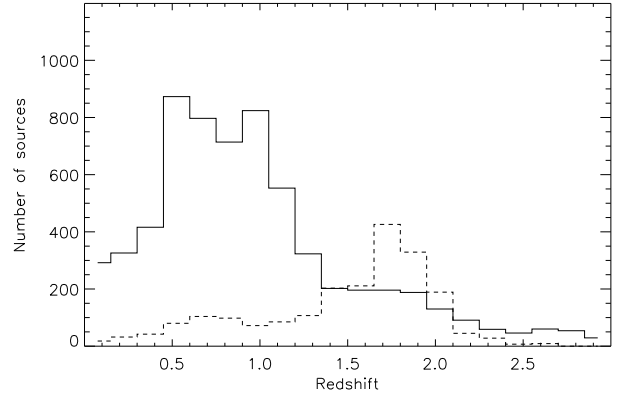


FIG. 2.— The redshift distribution of MIR sources is shown as a solid line for entries having a reliable photometric redshift assigned to them. The distribution peaks between $0.5 < z < 1$ and exhibits a substantial tail up to $z \sim 2$. The dashed histogram shows the distribution of sources with redshifts derived from the IRAC flux density ratios, which tend to cluster at $z \gtrsim 1$.

estimates. The photometric redshifts are based on data at similar wavelengths to those used by Brammer et al. (2008), but the algorithm itself differs from EAZY. Taylor et al. (2009) show that the two sets of redshift estimates are in equally good agreement with the available spectroscopic redshifts. However, this does not provide a method for deciding which methodology is more accurate for the optically dim, high-redshift sources which dominate in the submillimeter, and for which spectroscopic redshifts are much rarer. The photometric redshift error is estimated to be $\sigma_z \sim 0.06$ for both catalogs.

COMBO-17 photometric redshifts (Wolf et al. 2004, 2008) are available for the same sky region as MUSYC. The 5 broad and 12 narrow photometry bands from 350 to 930 nm enable accurate SED measurements, although the lack of near infrared data limits COMBO-17 capabilities to estimate redshifts reliably at $z \gtrsim 1.2$. The accuracy of these redshifts is $\sigma_z \sim 0.01$ for galaxies with $R < 21$, 0.02 for galaxies with $R \sim 22$ and 0.1 for those with $R > 24$, which is the sensitivity limit of the survey. Therefore, following other authors (e.g. Le Floch et al. 2005), we only use COMBO-17 sources with listed R magnitude brighter than 24.

Finally Rowan-Robinson et al. (2008) provide a catalog of photometric redshifts for the $24\ \mu\text{m}$ sources detected in SWIRE over a larger $4.56\ \text{deg}^2$ region within BGS-Wide, but with a shallower depth compared to FIDEL. The optical data ($g'r'i'$) are combined with the two shorter IRAC wavelengths, and are used to fit SED templates. The accuracy in σ_z is reported to be 0.035 and is comparable with the above catalogs.

3. REDSHIFTS OF MIPS SOURCES

The 9110 sources in the FIDEL catalog have positional accuracies that are significantly smaller than the MIPS PSF (Point Spread Function) at $24\ \mu\text{m}$. This is because the catalog positions are obtained from the more accurate near infrared (NIR) IRAC catalog. By matching the FIDEL and redshift catalogs we identified redshifts for $\sim 72\%$ of the FIDEL sources. We used a search radius of $1''$, but using $1.5''$ or $2''$ does not substantially change the number of identified sources. Given the surface densities of sources in the catalogs (MUSYC has one source every

190 arcsec² and MUSIC about one every 30 arcsec²), we expect only a few spurious associations within this search radius.

We identified redshifts from the catalogs in the following sequence: (i) FIREWORKS (18%); (ii) MUSYC (43%); (iii) MUSIC (1%); (iv) COMBO-17 (10%), and (v) the catalog of Rowan-Robinson et al. (2008) (0.5%). The redshift distribution (solid line in Figure 2) peaks at $z \sim 0.8$ and shows a high redshift tail which is particularly significant in the range $1.5 \lesssim z \lesssim 2$.

To determine redshifts for the remaining 28% of the MIR sources with no direct counterparts in the catalogs we used a relation between IRAC colors and redshifts similar to that derived in Devlin et al. (2009). Redshifts from FIREWORKS and MUSYC were matched to IRAC sources in the SIMPLE catalog. The resulting ~ 18000 objects were binned in a look-up table (LUT) as a function of IRAC flux density ratios. The table is shown in Figure 3 and exhibits a trend of increasing redshift from top-left to bottom-right. Redshifts for galaxies are assigned based on the mean values of sources that land in the same bin of the IRAC color-color plane with known redshifts.

A comparison between LUT-retrieved and known redshifts for a number of sources which have not been used to compile the table is shown in Figure 4. Although the trend is not linear and with a large scatter, the plot exhibits monotonic behavior and a reliable separation between low and high redshifts. Two plateaus are evident, one at $0.6 < z < 1.1$ and the other at $z > 1.6$.

We initially chose nine redshift bins spanning $0.016 < z < 3.5$ at logarithmically spaced intervals. The first three bins are narrower than the accuracy quoted for the redshift catalogs so we merged them to form a single bin 4% wide in $\Delta z / (1+z)$. We also merged the last two bins due to the small numbers of sources that landed within

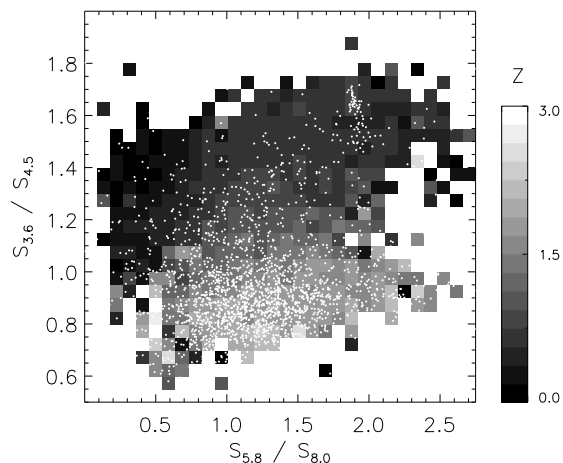


FIG. 3.— IRAC color-color plot of SIMPLE sources with redshifts. Pixels are grey-shaded according to redshift with lighter shades corresponding to higher redshifts. Overplotted as white dots are MIR galaxies in the FIDEL catalog for which no redshift information is available. These points cluster in the bottom region of the plane, showing that they are probably a population of high redshift sources. Redshifts were estimated for these objects directly from the means of sources with known redshifts that landed in the same bins of this color-color plane

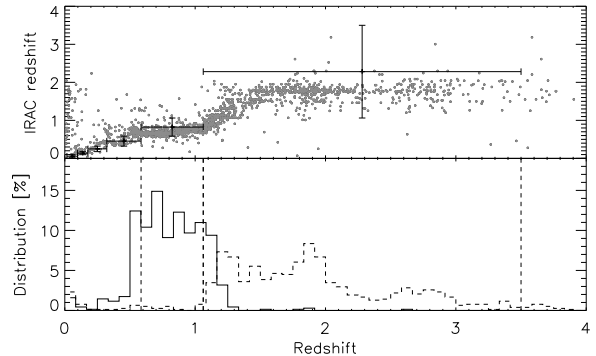


FIG. 4.— Robustness of IRAC redshifts derived from the NIR flux density ratios. The top panel compares the IRAC redshifts with the catalog of photometric redshifts. Although the relation is not linear, its monotonic trend can be used to assign sources to redshift bins, provided these are larger than the scatter introduced. The redshift binning grid is also shown with the crosses indicating the extension of each bin. The distribution of redshifts for sources whose redshift lies in the last two bins is shown in the bottom panel. The in-bin fraction is 68% and 90%.

them. The six final bins are overplotted in Figure 4. The redshift distribution for the sources selected in the last two bins from the IRAC LUT are also shown. Their widths are 68% and 90%, respectively. IRAC redshifts are not reliable in the lower-redshift bins.

Almost all 28% of the FIDEL sources with no redshifts have flux density ratios populating the bottom region of the IRAC plane, and their IRAC photometric redshift distribution (Figure 2) indicates that they lie preferentially at $z > 0.5$. This is also confirmed by studying the distribution of COMBO-17 redshifts for these sources. Although unreliable, as they are mostly $R \gtrsim 24$, the distribution peaks in the same redshift range.

In summary, we have obtained or calculated redshifts for 95% of the sources from the original MIPS catalog.

4. COMPLETENESS

The completeness of the flux-limited FIDEL catalog is investigated in Devlin et al. (2009), finding it to be 63, 80 and 96% complete at 20, 40, and 80 μJy , respectively. Marsden et al. (2009) have repeated their analysis and find compatible results. Ideally, one would like to have a similar completeness analysis for each redshift bin used here. Although it is tempting to apply the same corrections, in practice one should consider that the catalog is based on IRAC positions and it would be arbitrary to assume a one-to-one relation between sources missing in FIDEL and sources missing in the underlying SIMPLE catalog. In this work we have therefore ignored any completeness correction. We indicate what the expected effect might be in the analysis and discussions that follow.

5. STACKING ANALYSIS

Stacking analysis using positional information of sources selected at different wavelengths is a powerful tool for estimating the contribution from a given class of objects to the CIB at different wavelengths. In this paper we have considered the contribution of MIR selected sources to the CIB as a function of red-

TABLE 1
STACKED INTENSITIES

λ μm	Total	Total ^a ($z > 0$)	Total ^b ($z > 0$)	CIB ^c
	νI_ν [$\text{nW m}^2 \text{sr}^{-1}$]			
70	5.4 ± 0.3	5.2 ± 0.3	4.6 ± 0.3	...
250	8.2 ± 0.5	8.1 ± 0.5	6.1 ± 0.5	10.4 ± 2.3
350	4.8 ± 0.3	4.8 ± 0.3	3.3 ± 0.2	5.4 ± 1.6
500	2.0 ± 0.2	2.0 ± 0.2	1.2 ± 0.1	2.4 ± 0.6

NOTE. — Stacked intensities have not been corrected for completeness, and the quoted errors do not include calibration uncertainties. See Marsden et al. (2009) for the completeness corrected values.

^a Stacked intensity from every source with a redshift

^b Stacked intensity from every source with a redshift, excluding IRAC redshifts (see text in §3)

^c FIRAS measured background

shift at BLAST and *Spitzer* wavelengths. Our analysis follows the method of Dole et al. (2006). BLAST maps were whitened to suppress the larger scales not relevant to a point-source analysis. The whitening filter gain was taken into consideration when flux densities were measured. The region considered conservatively excludes the edges of the FIDEL and MUSYC area coverage. This region is described by a quadrilateral with corners at the following coordinates (J2000): $3^{\text{h}}31^{\text{m}}36^{\text{s}}$, $-28^{\circ}02'16''$; $3^{\text{h}}31^{\text{m}}29^{\text{s}}$, $-27^{\circ}38'34''$; $3^{\text{h}}33^{\text{m}}16^{\text{s}}$, $-27^{\circ}35'00''$; $3^{\text{h}}33^{\text{m}}26^{\text{s}}$, $-27^{\circ}58'50''$. 7280 FIDEL sources are in this region, compared to the total 9110 listed in the full catalog.

The means of each map in the stacking region are subtracted, as required by the stacking formulation. We then compile a list of postage-stamp maps centered at the position of each MIR source. These sub-maps are co-added and the total flux density evaluated with aperture photometry. Removing the mean locally before stacking is formally correct. We verified that the standard technique of subtracting the sky estimated in an annulus around the aperture gives a compatible result. Whitening the maps removes all significant large scale structure so that the postage-stamp maps can be co-added without rotating them, as in Dole et al. (2006). Although the SWIRE 70 μm map was not whitened, the filtering applied by the *Spitzer* reduction pipeline is strong enough to remove large scale fluctuations. We verified that the retrieved flux densities are the same both by stacking postage-stamp maps directly, and by alternately rotating them by 90° to mimic the analysis of Dole et al. (2006).

The total retrieved flux density can be overestimated if the distribution of MIR sources is clustered. Marsden et al. (2009) find this effect to be negligible and it is ignored in the subsequent analysis.

In order to validate the technique and to verify that the analysis pipeline does not introduce artifacts, stacking was performed on noiseless Monte Carlo simulations. Sky realizations were generated at 250 μm from model counts (Lagache et al. 2003). Source flux densities were drawn from the model and redshifts were assigned from a uniform distribution spanning $0 < z < 2$. Observed 24 μm flux densities were assigned to each galaxy using Arp 220 as a template to scale from the 250 μm flux densities given the redshifts. Only 24 μm flux densities brighter than 13 μJy were retained in this list.

We simulated time-stream detector data by scanning

the sky realizations with the actual BLAST telescope pointing solution. We then used the BLAST data reduction pipeline, identical to that for the real data, to generate maps.

Stacking was performed on the simulated sky realizations and on the maps obtained from the pipeline, and then compared to the total 250 μm flux density of the sources in the 24 μm mock catalog. The three measurements were found to agree within 2%, which is well within the errors.

A final test was carried out by stacking the FIDEL sources on the 24 μm *Spitzer* map. Again, we found that the retrieved flux density was in good agreement with the total flux density in the list.

The uncertainties are estimated as in Marsden et al. (2009) and a similar check for Gaussianity was performed. We also verified that stacking against a catalog of randomly selected positions returns a stacked value of zero.

Our stacking region covers a fairly small area of 590 arcmin². Sampling variance plays an important role, with Dole et al. (2006) suggesting that it can be as large as a factor of 2 (peak-to-peak). Although we do not presently have comparable data in a different field with which to test this hypothesis, we make a rough estimate by dividing the present field into 4 separate pieces of roughly equal areas. Stacking in each of these regions independently we find an RMS dispersion of $\sim 15\%$ in the retrieved flux densities, which is fairly correlated among the different BLAST and *Spitzer* wavebands. Therefore the final RMS variation is expected to be a factor of 2 smaller than this, although it is not explicitly used in the error bars later in this analysis. This is a lower limit on the sampling variance as this calculation can not account for scales larger than 1/4 of the map.

Table 1 lists the results of this analysis. The 70 μm retrieved intensity is compatible with values from Dole et al. (2006) and Dye et al. (2007). At the BLAST wavelengths these values are within 6% of the ones reported by Devlin et al. (2009), and within 4% of those in Marsden et al. (2009).

The stacked intensities for the 5% of sources with no redshift information is negligible compared to the total ($< 3\%$). The table also lists flux densities retrieved using only sources with redshifts obtained directly from the catalogs (i.e. no IRAC redshifts). These flux densities are 10%, 30%, 30%, and 40% lower at wavelengths 70, 250, 350, and 500 μm , respectively. This is broadly expected if the excluded sources lie at high redshift, such that the longer wavelengths are more seriously affected. It also provides a consistency check for the IRAC redshift method discussed earlier.

Although the stacked flux density as a function of wavelength is compatible with the FIRAS detection, given its large error and the sampling variance, it is still possible that a missing population of faint 24 μm sources is needed to resolve the CIB completely. This is argued in Marsden et al. (2009), and will be discussed further in later sections. In any case, it is worth noting that existing estimates of the total resolved CIB are highly uncertain, and FIRAS measurements can be affected by systematics and have a formal error of 25%.

The observed CIB is the total dust reprocessed starlight produced in galaxies at all redshifts and luminosities. Splitting the FIDEL catalog into redshifts bins is an effective way to study the contribution that each sub-catalog has to the total intensity. The redshift bins used (see §3) were chosen to be at least $1\sigma_z$ or larger in $\Delta z/(1+z)$, and the width of the last two bins ensures that the errors in the IRAC redshifts do not result in sources being placed in the wrong bin (Figure 4). The mean stacked intensity in each bin is listed in Table 2.

The cumulative distribution of stacked intensities is shown in Figure 5 as a function of both $24\mu\text{m}$ flux density and redshift, and it is normalized to the total intensity listed in Table 1. We prefer this normalization over the FIRAS measurements because i) there is no $70\mu\text{m}$ FIRAS detection and the most accurate detections of the CIB at this wavelength are lower limits, ii) the FIRAS detections in the BLAST bands have large uncertainties, and iii) the BLAST survey is affected by sampling variance making it difficult to compare with an all sky survey.

A similar qualitative behavior is seen in both panels of Figure 5, with the stacking measurements at shorter wavelengths dominating the brighter $24\mu\text{m}$ flux densities and the lower redshifts. By redshift 1.1, about 75% of the CIB is generated at $70\mu\text{m}$, 55% at $250\mu\text{m}$, 45% at $350\mu\text{m}$, and 40% at $500\mu\text{m}$. Similar results are found by Marsden et al. (2009) who estimate these fractions to be 50, 45, and 40% at 250, 350, and $500\mu\text{m}$, respectively (although $z = 1.2$ is used there). The relatively small discrepancy can be accounted for by the different way redshifts are assigned. In this work, most redshifts have been retrieved from catalogs, while Marsden et al. (2009) only uses a rough division into two redshift bins using IRAC colors.

Wang et al. (2006) find similar results stacking IRAC selected sources in the $850\mu\text{m}$ map of the GOODS-N field, with a 50% fraction of their total stacked back-

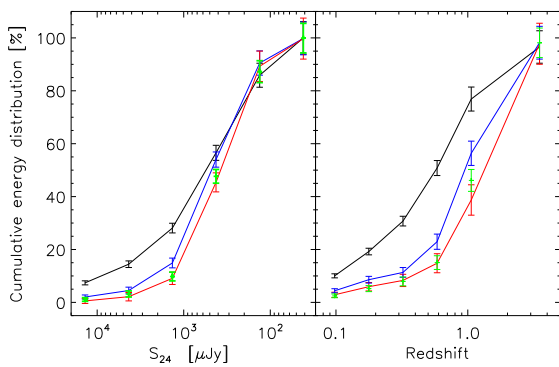


FIG. 5.— The cumulative energy distribution is shown as a function of $24\mu\text{m}$ flux density (left panel) and redshift (right panel) for *Spitzer* at $70\mu\text{m}$, in black, and BLAST in blue ($250\mu\text{m}$), green ($350\mu\text{m}$) and red ($500\mu\text{m}$). Each curve shows the integrated stacked intensity normalized to the total stacked intensity at each wavelength as listed in Table 1. Different wavelengths contribute most to the CIB at different epochs, or at different $24\mu\text{m}$ flux densities, with most of the $70\mu\text{m}$ background being generated at $z \lesssim 1$ and the $500\mu\text{m}$ background at higher redshifts. The cumulative plot as a function of flux density shows a similar trend at all wavelengths, suggesting that brighter $24\mu\text{m}$ sources are likely to be at lower redshifts.

ground (which is 50–75% of the FIRAS background) generated at $z > 1.5$.

It is worth mentioning that the fractions of resolved background depend on the normalization adopted. If FIRAS is used instead, all of these fractions change by as much as 20% at the BLAST wavelengths (not accounting for the quoted measurement uncertainties).

Compared to $70\mu\text{m}$, the $500\mu\text{m}$ cumulative distribution shows no evidence of convergence in the highest redshift bin, suggesting that a population of faint $24\mu\text{m}$ sources is missing to fully resolve the CIB at the longer wavelengths.

7. AVERAGE PHYSICAL PARAMETERS

The average flux densities at 70, 250, 350, and $500\mu\text{m}$ from stacking (total stack divided by the number of contributing sources) were used to fit SEDs in each redshift interval to estimate the average bolometric luminosities (from 8 to $1000\mu\text{m}$ in the rest frame) of the MIR sources as a function of z .

Since the emission mechanism at these wavelengths is thermal, the natural choice of SED is a modified greybody with some emissivity law: $A\nu^\beta B(\nu, T)$, where $B(\nu, T)$ is the blackbody spectrum and A its amplitude. Such a model assumes a single dust temperature, but the reality is far more complex. Temperature distributions are observed both within single galaxies and among different sources. As a consequence, the resulting spectrum is better described by a power law than a Wien exponential decay at wavelengths shorter than the peak in the SED. Indeed, for our data modified greybody fit the combined *Spitzer* $70\mu\text{m}$ and BLAST data points progressively poorer with increasing redshift, as the $70\mu\text{m}$ channel samples shorter rest-frame wavelengths.

The fitting template we used instead is a modified greybody with a fixed emissivity index $\beta = 1.5$, and a power law decay $\nu^{-\alpha}$ at short wavelengths to prevent the high-frequency SED from falling exponentially. The exponent α is chosen by fitting the SEDs of two often used galaxies: the Ultra Luminous IR Galaxy (ULIRG, $L > 10^{12} L_\odot$, $\alpha = 2.8$) Arp 220, and the Luminous IR galaxy (LIRG, $L > 10^{11} L_\odot$, $\alpha = 1.8$) M82. The former is a merging system, and the latter is a starburst triggered by tidal encounters with the nearby spiral M81. The fit estimates the amplitude of the template and the temperature, keeping α and β fixed. Both SEDs fit the four data points at each redshift, as shown in Figure 6 for the $\alpha = 2.8$ model.

The estimate of bolometric luminosity (the integral from 8 to $1000\mu\text{m}$ of the SED in the rest-frame) is a weak function of the template (Figure 7), emphasizing that the model need only provide a reasonable interpolation of the data around the peak of the rest-frame FIR emission. The retrieved luminosities increase steeply with redshift. The top panel in Figure 7 plots the mean bolometric luminosity as a function of the redshift. It is in good agreement with a similar result found by Le Floch et al. (2005), who studied the evolution of bolometric luminosities for the same population of $24\mu\text{m}$ sources, although with a higher MIR flux density limit of $80\mu\text{Jy}$. The figure provides an estimate of the selection effect arising from the flux density limit of the FIDEL catalog, which we assume is $20\mu\text{Jy}$, the 63% completeness limit. The calculation uses template models for “normal” and “star-

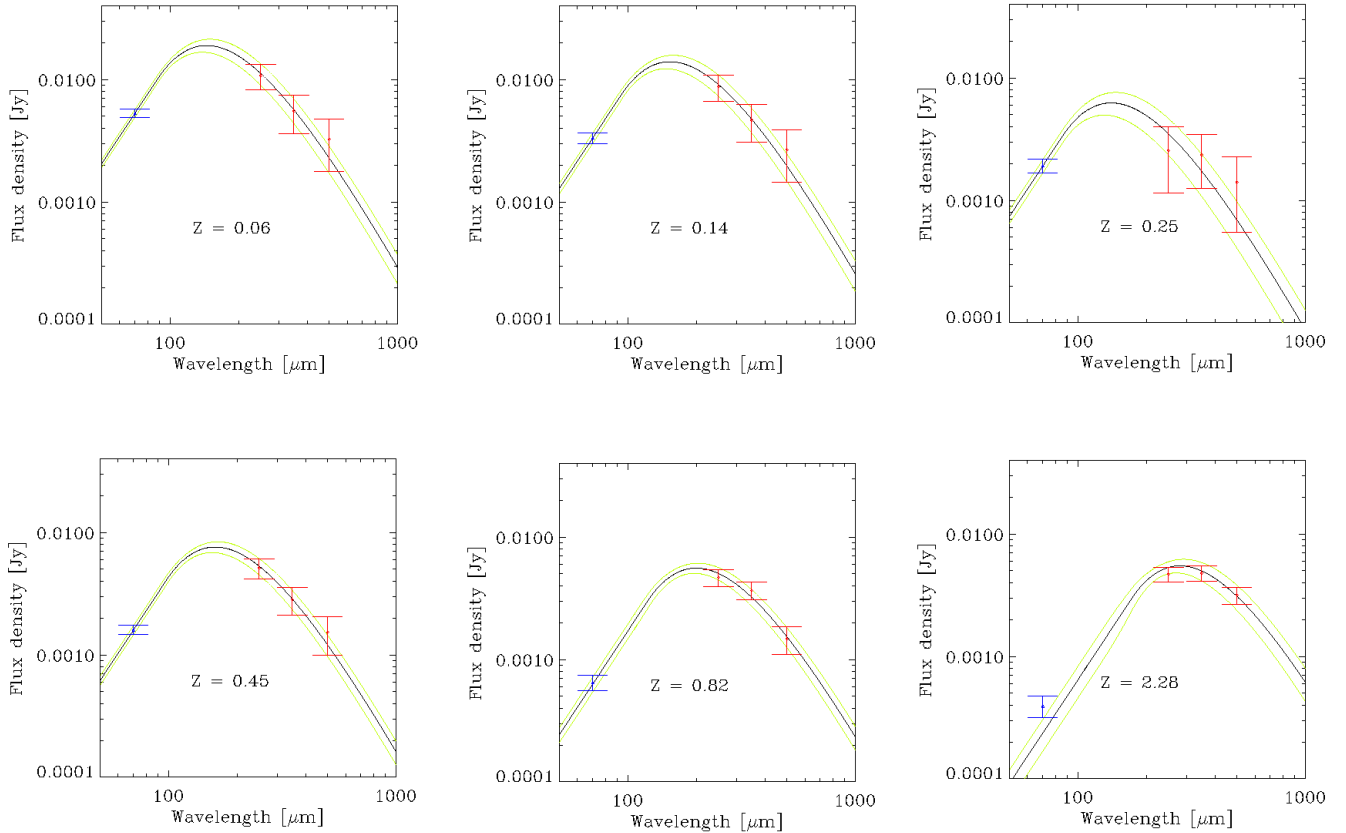


FIG. 6.— SED fitting of the average flux densities measured in different redshift bins. Black solid lines: best fits; green solid lines: 68% confidence levels; red points with error bars: BLAST detections after color correction; blue point with error bars: *Spitzer* 70 μm . The fit accounts for the finite BLAST bandwidths and for the correlated calibration uncertainties. The model template is a modified greybody with an emissivity law $\beta = 1.5$ and a power law $\nu^{-\alpha}$ replacing the Wien part of the spectrum. Two templates were used: one with $\alpha = 2.8$, describing Arp 220’s spectrum, and one with $\alpha = 1.8$ which is better matched to M82. Both models are compatible with the data, although only the $\alpha = 2.8$ fit is shown here for clarity.

burst” galaxies from Lagache et al. (2003), co-added after first normalizing to the same bolometric luminosity.

As shown in Kennicutt (1998), the FIR emission is tightly correlated with star formation activity (Star Formation Rate, or SFR), under the assumption that star formation is completely optically obscured by dust and that the fraction of infrared luminosity dominated by AGN heating is negligible¹³. The relation between bolometric luminosity and dust obscured SFR is then:

$$\text{SFR}[\text{M}_{\odot} \text{yr}^{-1}] = 1.728 \times 10^{-10} L [L_{\odot}].$$

This relationship is used to calibrate the SFR axes of the luminosity plots.

From Figure 7, we observe that at low redshifts ($z \lesssim 0.6$) the MIR population is dominated by moderate IR emitters ($L \lesssim 6 \times 10^{10} L_{\odot}$). As the redshift increases, the volume probed also increases and LIRGS become more common, which is consistent with many spheroids being formed at about this time ($z \sim 1$). This is expected, as SCUBA surveys at 850 μm have revealed the existence of a large number of ULIRG-type objects, residing

¹³ Devlin et al. (2009) show that the AGN contribution to the CIB at BLAST wavelengths is about 7%, and it is small enough to be ignored.

at typically higher redshifts with a median of $z \sim 2.5$ (Chapman et al. 2003).

We emphasize once more that the quantities estimated are the average values of the population of MIR sources resolving most, if not all, of the CIB detected by FIRAS.

The last bin in Figure 7 probes a redshift range similar to the SCUBA galaxies. However, the mean luminosity is slightly lower than that typically quoted for SCUBA galaxies suggesting either that some of the most luminous objects (and potentially most optically obscured) are missing from the bin, or that SCUBA galaxies have luminosities that are above average at those redshifts.

Our template fitting returns rest-frame temperatures, but these are more model-dependent than the luminosities. As shown in Figure 7, the difference in the temperatures determined for the two templates is about 5 K across the whole redshift range.

We observe an increase in mean temperature. This trend can be explained by the correlation observed between temperature and luminosity as discussed by Dunne et al. (2000). Detailed modeling beyond the scope of this paper would be required to determine whether selection or cosmic evolution also play a role.

The average mass in dust can be estimated from the

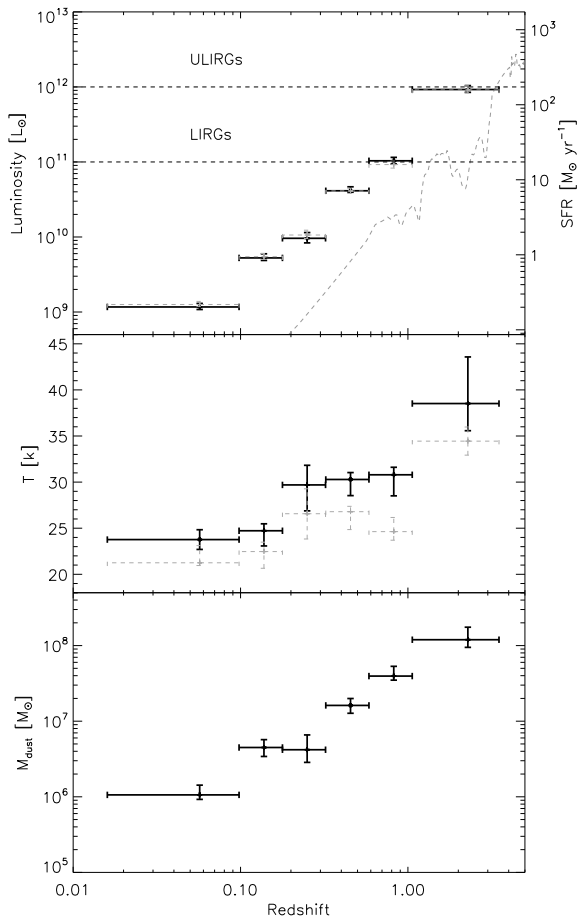


FIG. 7.— The mean rest-frame luminosities, temperatures and dust masses of the MIR FIDEL sources are plotted against redshift. In the top panel, the mean bolometric luminosities are estimated from the $\alpha = 2.8$ (black points) and the $\alpha = 1.8$ (grey, dashed points) SED fits. There is little difference between the two, confirming that the estimated luminosities are a weak function of the template used. The grey line provides an estimate of selection arising from a $24 \mu\text{m}$ flux density limit of $20 \mu\text{Jy}$ (63% completeness limit of the catalog). The mid panel shows rest-frame temperatures for both templates. A difference of ~ 5 K is observed between the two, with temperatures increasing with redshift. Dust masses are calculated assuming a constant, mean rest-frame temperature of 30 K, to account for the unreliably fitted temperatures.

observed flux densities (Hildebrand 1983), S_{ν_0} :

$$M_d = \frac{D_L^2(z)}{1+z} \frac{S_{\nu_0}}{k_{\nu_0(1+z)} B[\nu_0(1+z), T]}$$

where D_L is the luminosity distance. The mass-absorption coefficient, k_ν , is evaluated at 1 mm ($k_{1\text{mm}} = 0.1 \text{ m}^2 \text{ kg}^{-1}$, Hughes 1996) and has a ν^β dependence. Any dust mass estimate has to be treated with caution because i) $k_{1\text{mm}}$ is uncertain within an order of magnitude (Blain et al. 2002), and ii) the temperature is largely uncertain. To limit the impact of uncertainties in the temperature on inferred dust masses, we use the flux density at a rest-frame wavelength of $500 \mu\text{m}$ and a

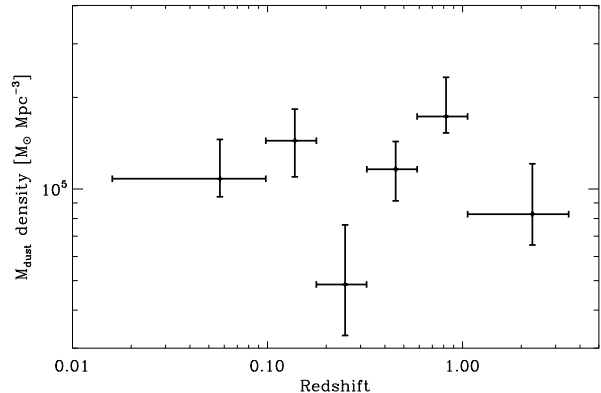


FIG. 8.— Comoving dust mass density vs. redshift. There is no evidence of significant evolution with redshift.

fixed temperature of 30 K. The dust mass shows a steady increase over two orders of magnitude across the probed range of redshifts.

8. LUMINOSITY AND STAR FORMATION HISTORIES

Mean rest-frame bolometric luminosities and dust masses can be converted into comoving-volume densities. The conversion factor applied to each redshift bin is the ratio of the number of sources in the bin to the comoving-volume probed by the bin, which, for a Euclidean geometry, we calculate as

$$V_{\text{com}}(\bar{z}) = \frac{\Omega_{\text{stack}}}{3} \left[\frac{D_L^3(z_{\text{hi}})}{(1+z_{\text{hi}})} - \frac{D_L^3(z_{\text{lo}})}{(1+z_{\text{lo}})} \right].$$

Here, Ω_{stack} is the solid angle of the stacking region, z_{lo} and z_{hi} are the edges of each redshift interval, and \bar{z} is the bin center.

Interestingly, the comoving dust mass densities shown in Figure 8 do not exhibit substantial variation (within a factor of 10). This suggests that the amount of comoving dust associated with the FIDEL sources is fairly constant as galaxies are built up. Dunne et al. (2003) found that there was much more dust at $z \gtrsim 1$, although their survey is only sensitive to galaxies with very large dust masses, whereas our stacking analysis is sensitive to galaxies with a wider range of dust masses.

The comoving FIR luminosity densities are shown in Figure 9 and are listed in Table 2. The left vertical axis is converted into star formation rate density. We used the template with $\alpha = 2.8$ to calculate the luminosities. Also shown is the effect of excluding sources for which redshifts from the IRAC color-color plane have been obtained. This affects mostly the higher redshift bin. We note once again that the error bars include only the statistical uncertainties arising from the stacking and calibration and do not include the effect of sampling variance. This plot is a complete representation of the energetics in the CIB generated by MIR sources at the FIDEL flux density limit, as 95% of these galaxies have been included and the remaining 5% do not contribute substantially to the background. The luminosity density plot shows the luminosity integrated over the comoving volume. A naïve model is overplotted (not fitted) and is derived from the Saunders et al. (1990) luminosity

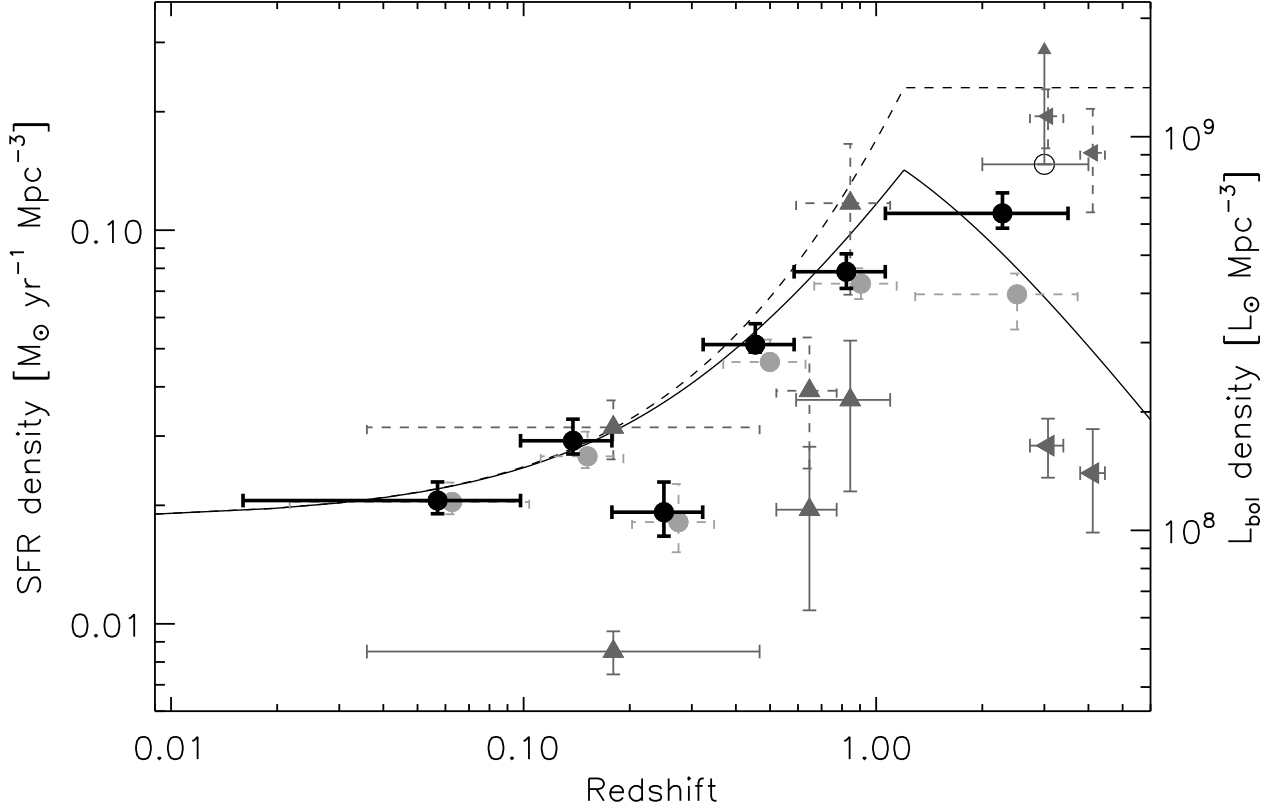


FIG. 9.— The evolution of the total bolometric luminosity density up to $z = 3.5$ from MIR-selected sources is shown as black filled circles. The other points are optical-UV detections from Lilly et al. (1996) (up-pointing solid triangles) and Steidel et al. (1999) (left-pointing solid triangles). The corresponding symbols with dashed error bars are the extinction-corrected values. The open circle is the lower limit of Hughes et al. (1998) derived for SCUBA galaxies. SFR is shown on the left axis and shows good agreement with the optical extinction corrected estimates, confirming that most of the star-forming activity in the Universe is obscured by dust. The light grey filled circles, with dashed error bars, are calculated from the same MIR population, from which the sources with redshifts estimated from IRAC colors have been removed, and are shifted by 10% in both z and luminosity for visual clarity. A luminosity function model (not a fit) is plotted as a solid line, and it is also evaluated at a $24\ \mu\text{m}$ flux density limit of $20\ \mu\text{Jy}$ to indicate the effect of the FIDEL catalog flux density limit (dashed line). The last redshift bin falls low compared with the SCUBA lower limit (and the extinction-corrected point at similar redshift), and suggests that a fraction of SCUBA galaxies might be a population of faint $24\ \mu\text{m}$ sources missing from the FIDEL sample.

TABLE 2
STACKING ANALYSIS RESULTS

z_{lo}	z_{hi}	$\nu I_\nu(70\ \mu\text{m})$	$\nu I_\nu(250\ \mu\text{m})$	$\nu I_\nu(350\ \mu\text{m})$	$\nu I_\nu(500\ \mu\text{m})$
nW m ² sr ⁻¹					
0.016	0.098	0.53 ± 0.04	0.31 ± 0.07	0.11 ± 0.04	0.05 ± 0.02
0.098	0.177	0.49 ± 0.04	0.36 ± 0.08	0.13 ± 0.04	0.06 ± 0.03
0.177	0.322	0.54 ± 0.06	0.20 ± 0.11	0.13 ± 0.06	0.06 ± 0.03
0.322	0.585	1.31 ± 0.11	1.19 ± 0.19	0.45 ± 0.10	0.19 ± 0.06
0.585	1.062	1.26 ± 0.16	2.53 ± 0.30	1.38 ± 0.16	0.42 ± 0.09
1.062	3.500	1.06 ± 0.19	3.45 ± 0.35	2.51 ± 0.18	1.22 ± 0.11

L_{min} is set to zero in one case (dashed curve) to show the total bolometric luminosity density predicted by this model. The solid curve was calculated for L_{min} estimated assuming a $24\ \mu\text{m}$ flux density of $20\ \mu\text{Jy}$ (63% completeness) and our fitting template, and shows the effect of the flux density limit in the FIDEL catalog (higher flux density limits correspond to larger values of L_{min}). The evolution was chosen to be $f(z) = (1+z)^{3.2}$ up to $z = 1.2$, and constant at higher redshifts. This naïve modeling shows good agreement with the data and qualitatively demonstrates the effect of the flux density limit of the catalog. As expected, the only substantial change is to the highest redshift point.

function (LF) form for IRAS galaxies,

$$\Phi_{\text{IR}}(L) = \phi_{\text{IR}}^* \left(\frac{L}{L_{\text{IR}}^*} \right)^{1-\alpha_{\text{IR}}} e^{-\frac{1}{2\sigma_{\text{IR}}^2} \log^2 \left[1 + \frac{L}{L_{\text{IR}}^*} \right]}.$$

The coefficients adopted for this model are from Le Floc'h et al. (2005) for a fit to the local bolometric LF. The quantity plotted is then

$$\frac{dL}{dV_{\text{com}}} = \int_{L_{\text{min}}}^{\infty} L \Phi_{\text{IR}} \left(\frac{L}{f(z)} \right) d \log L.$$

The bolometric luminosity densities estimated here show good agreement with the extinction corrected results obtained from optical detections (Lilly et al. 1996) at ($z \lesssim 1$). As the MIR sources resolve most, if not all, of the CIB, at its emission peak, this is the first direct measurement of its energetics and of the dust obscured star formation history of the Universe. Although the agreement with previous measurements is remarkably good, previous studies have had to rely on modeling of dust

obscuration and SEDs to evaluate bolometric luminosities. With the combination of BLAST and *Spitzer*, we have been able to directly probe this quantity without any assumption of the underlying physical details.

Comparing our measurements with the optical measurements (the triangle symbols with solid error bars in Figure 9), we find that the fraction of light from young stars hidden by dust is about 70% in the range $0.1 < z < 1$.

The highest redshift bin, which coincides with the redshifts at which SCUBA galaxies are typically found, is the most affected by the FIDEL flux density limit. Comparing with the lower limit on the SFR density for SCUBA galaxies of Hughes et al. (1998), it appears as if some fraction of this population is missing from the FIDEL catalog, which does not contain large fractions of ULIRG-type objects as discussed in the previous section. It is possible that a significant fraction of SCUBA galaxies have fainter $24\ \mu\text{m}$ flux densities than the threshold we used for the FIDEL catalog, although we note that many SCUBA sources have had $24\ \mu\text{m}$ counterparts identified in past surveys (e.g. Pope et al. 2006; Ivison et al. 2007). It also may be possible that some of the high-redshift sources in our catalog have simply been mis-identified as lower-redshift objects, but due to their relatively small numbers, have little effect on the lower-redshift bins.

Either way, there is evidence that this study misses a portion of the SFR history at the highest redshifts during which it is believed the most massive galaxies were forming through powerful mergers. This is consistent with the result of Marsden et al. (2009) who find the contribution of FIDEL sources to the CIB at $850\ \mu\text{m}$ to be significantly low compared to the FIRAS measurements. They also find that their estimate of the CIB generated at $850\ \mu\text{m}$ by sources with $z > 1.2$ is low compared to the model of Valiante et al. (2009) which otherwise fits the CIB at the BLAST wavelengths.

9. CONCLUSIONS

We have studied the contribution of MIR galaxies selected at $24\ \mu\text{m}$ to the CIB and found that they resolve most, if not all, of the radiation detected by the all-sky FIRAS and DIRBE surveys at the peak of the far infrared background. We assigned redshifts to more than 70% of this population from existing redshift catalogs, and developed a technique which uses the NIR IRAC colors to assign redshifts to the remainder of the catalog. Using a stacking analysis to overcome the confusion noise arising from the finite instrumental resolution, we study

the composition of the CIB as a function of redshift. We find that 60% of the CIB at $500\ \mu\text{m}$ is generated at redshifts $z > 1.1$ while the $70\ \mu\text{m}$ background has a more recent origin, with 75% of it being generated at redshifts $z < 1.1$.

By fitting SEDs to the mean flux densities at each redshift, we have shown that, on average, this population is consistent with being predominantly lower-luminosity LIRGs than the ULIRGs detected in SCUBA surveys. It appears that a significant fraction of the SCUBA galaxies known to exist redshifts $z > 2$ are missing from our analysis, and we conjecture that they are simply below the $24\ \mu\text{m}$ flux density limit in our source catalog, or in some cases have had their redshifts mis-identified. However, while such objects are important at high redshifts, their contribution to the peak of the CIB is small compared with the bulk of the MIR-selected galaxies at lower redshifts.

The evolution in the total comoving bolometric luminosity density is evaluated using MIPS and BLAST data directly as these wavelengths span the rest-frame FIR peak emission. This evolution is then directly converted into the star formation rate history. We find good agreement with existing studies conducted at optical-UV wavelengths which have had to rely on many more assumptions about physical source properties.

Our results confirm that dust obscuration dominates the history of star formation of the Universe, with star formation rates that are about three times larger than in the optical-UV, in the redshift range $0.1 < z < 1$.

These results can be used to constrain models of luminosity densities and galaxy formation as they directly probe the FIR energetics of the Universe up to redshift $z \sim 3$.

10. ACKNOWLEDGEMENTS

We acknowledge the support of NASA through grant numbers NAG5-12785, NAG5-13301, and NNGO-6GI11G, the NSF Office of Polar Programs, the Canadian Space Agency, the Natural Sciences and Engineering Research Council (NSERC) of Canada, and the UK Science and Technology Facilities Council (STFC). This work is based in part on observations made with the *Spitzer* Space Telescope, which is operated by the Jet Propulsion Laboratory, California Institute of Technology under a contract with NASA.

The authors are grateful to Hervé Dole for fruitful suggestions on the analysis, and to Benjamin Magnelli for help with the FIDEL $24\ \mu\text{m}$ data.

REFERENCES

- Blain, A. W., Smail, I., Ivison, R. J., Kneib, J.-P., & Frayer, D. T. 2002, *Phys. Rep.*, 369, 111
- Brammer, G. B., van Dokkum, P. G., & Coppi, P. 2008, *ApJ*, 686, 1503
- Chapman, S. C., Blain, A. W., Ivison, R. J., & Smail, I. R. 2003, *Nature*, 422, 695
- Damen, M., Labbé, I., Franx, M., van Dokkum, P. G., Taylor, E. N., & Gawiser, E. J. 2009, *ApJ*, 690, 937
- Devlin, M. J., Ade, P. A. R., Aretxaga, I., Bock, J. J., Chapin, E. L., Griffin, M., Gundersen, J. O., Halpern, M., et al. 2009, *Nature*, 458, 737
- Dole, H., Lagache, G., Puget, J.-L., Caputi, K. I., Fernández-Conde, N., Le Floch, E., Papovich, C., Pérez-González, P. G., et al. 2006, *A&A*, 451, 417
- Dunne, L., Eales, S., Edmunds, M., Ivison, R., Alexander, P., & Clements, D. L. 2000, *MNRAS*, 315, 115
- Dunne, L., Eales, S. A., & Edmunds, M. G. 2003, *MNRAS*, 341, 589
- Dwek, E., Arendt, R. G., Hauser, M. G., Fixsen, D., Kelsall, T., Leisawitz, D., Pei, Y. C., Wright, E. L., et al. 1998, *ApJ*, 508, 106
- Dye, S., Eales, S. A., Ashby, M. L. N., Huang, J.-S., Egami, E., Brodwin, M., Lilly, S., & Webb, T. 2007, *MNRAS*, 375, 725
- Dye, S. et al. 2009, *ApJ*, submitted, arXiv:0904.1204v1 [astro-ph.CO]
- Fixsen, D. J., Dwek, E., Mather, J. C., Bennett, C. L., & Shafer, R. A. 1998, *ApJ*, 508, 123

- Grazian, A., Fontana, A., de Santis, C., Nonino, M., Salimbeni, S., Giallongo, E., Cristiani, S., Gallozzi, S., et al. 2006, *A&A*, 449, 951
- Griffin, M. J., Swinyard, B. M., & Vigroux, L. G. 2003, in Presented at the Society of Photo-Optical Instrumentation Engineers (SPIE) Conference, Vol. 4850, IR Space Telescopes and Instruments. Edited by John C. Mather. Proceedings of the SPIE, Volume 4850, pp. 686-697 (2003), ed. J. C. Mather, 686–697
- Hildebrand, R. H. 1983, *QJRAS*, 24, 267
- Hughes, D. H. 1996, in *Astrophysics and Space Science Library*, Vol. 206, Cold Gas at High Redshift, ed. M. N. Bremer & N. Malcolm, 311–+
- Hughes, D. H., Serjeant, S., Dunlop, J., Rowan-Robinson, M., Blain, A., Mann, R. G., Ivison, R., Peacock, J., et al. 1998, *Nature*, 394, 241
- Ivison, R. J., Greve, T. R., Dunlop, J. S., Peacock, J. A., Egami, E., Smail, I., Ibar, E., van Kampen, E., et al. 2007, *MNRAS*, 380, 199
- Kennicutt, Jr., R. C. 1998, *ARA&A*, 36, 189
- Lagache, G., Dole, H., & Puget, J.-L. 2003, *MNRAS*, 338, 555
- Le Floc'h, E., Papovich, C., Dole, H., Bell, E. F., Lagache, G., Rieke, G. H., Egami, E., Pérez-González, P. G., et al. 2005, *ApJ*, 632, 169
- Lilly, S. J., Le Fevre, O., Hammer, F., & Crampton, D. 1996, *ApJ*, 460, L1+
- Lonsdale, C. J., Smith, H. E., Rowan-Robinson, M., Surace, J., Shupe, D., Xu, C., Oliver, S., Padgett, D., et al. 2003, *PASP*, 115, 897
- Marsden, G., Ade, P. A. R., Benton, S., Bock, J. J., Chapin, E. L., Chung, J., Devlin, M. J., Dicker, S., et al. 2008, in *Society of Photo-Optical Instrumentation Engineers (SPIE) Conference Series*, Vol. 7020, Society of Photo-Optical Instrumentation Engineers (SPIE) Conference Series
- Marsden, G. et al. 2009, *ApJ*, submitted, arXiv:0904.1205v1 [astro-ph.CO]
- Papovich, C., Dole, H., Egami, E., Le Floc'h, E., Pérez-González, P. G., Alonso-Herrero, A., Bai, L., Beichman, C. A., et al. 2004, *ApJS*, 154, 70
- Pascale, E., Ade, P. A. R., Bock, J. J., Chapin, E. L., Chung, J., Devlin, M. J., Dicker, S., Griffin, M., et al. 2008, *ApJ*, 681, 400
- Patanchon, G., Ade, P. A. R., Bock, J. J., Chapin, E. L., Devlin, M. J., Dicker, S., Griffin, M., Gundersen, J. O., et al. 2008, *ApJ*, 681, 708
- Pope, A., Scott, D., Dickinson, M., Chary, R.-R., Morrison, G., Borys, C., Sajina, A., Alexander, D. M., et al. 2006, *MNRAS*, 370, 1185
- Puget, J.-L., Abergel, A., Bernard, J.-P., Boulanger, F., Burton, W. B., Desert, F.-X., & Hartmann, D. 1996, *A&A*, 308, L5+
- Rowan-Robinson, M., Babbedge, T., Oliver, S., Trichas, M., Berta, S., Lonsdale, C., Smith, G., Shupe, D., et al. 2008, *MNRAS*, 386, 697
- Saunders, W., Rowan-Robinson, M., Lawrence, A., Efstathiou, G., Kaiser, N., Ellis, R. S., & Frenk, C. S. 1990, *MNRAS*, 242, 318
- Steidel, C. C., Adelberger, K. L., Giavalisco, M., Dickinson, M., & Pettini, M. 1999, *ApJ*, 519, 1
- Taylor, E. N., Franx, M., van Dokkum, P. G., Quadri, R. F., Gawiser, E., Bell, E. F., Barrientos, L., Blanc, G. A., et al. 2009, ArXiv e-prints
- Truch, M. D. P., Ade, P. A. R., Bock, J. J., Chapin, E. L., Devlin, M. J., Dicker, S., Griffin, M., Gundersen, J. O., et al. 2009, *ApJ*, submitted, arXiv:0904.1202v1 [astro-ph.IM]
- Truch, M. D. P., Ade, P. A. R., Bock, J. J., Chapin, E. L., Devlin, M. J., Dicker, S., Griffin, M., Gundersen, J. O., et al. 2008, *ApJ*, 681, 415
- Valiante, E. et al. 2009, *ApJ*, submitted
- Wang, W.-H., Cowie, L. L., & Barger, A. J. 2006, *ApJ*, 647, 74
- Wolf, C., Hildebrandt, H., Taylor, E. N., & Meisenheimer, K. 2008, ArXiv e-prints
- Wolf, C., Meisenheimer, K., Kleinheinrich, M., Borch, A., Dye, S., Gray, M., Wisotzki, L., Bell, E. F., et al. 2004, *A&A*, 421, 913
- Wuyts, S., Labbé, I., Schreiber, N. M. F., Franx, M., Rudnick, G., Brammer, G. B., & van Dokkum, P. G. 2008, *ApJ*, 689, 653